ADVANCED ENERGY MATERIALS
www.advenergymat.de

One-Step Synthesis of 2-Ethylhexylamine Pillared Vanadium Disulfide Nanoflowers with Ultralarge Interlayer Spacing for High-Performance Magnesium Storage

*Xiaolan Xue, Renpeng Chen, Changzeng Yan, Peiyang Zhao, Yi Hu, Weihua Kong, Huinan Lin, Lei Wang, and Zhong Jin**

Rechargeable magnesium batteries (RMBs) are attractive candidates for large-scale energy storage owing to the high theoretical specific capacity, rich earth abundance, and good safety characteristics. However, the development of desirable cathode materials for RMBs is constrained by the high polarity and slow intercalation kinetics of Mg^{2+} ions. Herein, it is demonstrated that 2-ethylhexylamine pillared vanadium disulfide nanoflowers (expanded VS_2) with enlarged interlayer distances exhibit greatly boosted electrochemical performance as a cathode material in RMBs. Through a one-step solution-phase synthesis and in situ 2-ethylhexylamine intercalation process, VS_2 nanoflowers with ultralarge interlayer spacing are prepared. A series of ex situ characterizations verify that the cathode of expanded VS_2 nanoflowers undergoes a reversible intercalation reaction mechanism, followed by a conversion reaction mechanism. Electrochemical kinetics analysis reveal a relatively fast Mg-ion diffusivity of expanded VS_2 nanoflowers in the order of 10^{-11}–10^{-12} cm^2 s^{-1}, and the pseudocapacitive contribution is up to 64% for the total capacity at 1 mV s^{-1}. The expanded VS_2 nanoflowers show highly reversible discharge capacity (245 mAh g^{-1} at 100 mA g^{-1}), good rate capability (103 mAh g^{-1} at 2000 mA g^{-1}), and stable cycling performance (90 mAh g^{-1} after 600 cycles at 1000 mA g^{-1}).

1. Introduction

The exploitation of secondary batteries based on metal lithium anodes is seriously plagued by the safety issues rooted in the formation of lithium dendrites.[1–5] As an alternative, rechargeable magnesium batteries (RMBs) with metal Mg anodes have recently received great attention owing to the cost efficiency, abundant reserves, and dendrite-free plating process. Notably, magnesium also gives a theoretical volumetric capacity of 3833 mAh cm^{-3} nearly double that of lithium (2062 mAh cm^{-3}), and exhibits a relatively negative reduction potential of −2.4 V versus standard hydrogen electrode (SHE).[6–9] Despite of these intriguing merits, the practical employment of RMBs is hampered by several main hurdles. First, clumsy Mg^{2+} intercalation is the primary limitation for the choice of competent cathode materials, because the strong Coulombic interactions between the divalent Mg^{2+} ions and the anions in the host materials often result in sluggish diffusion kinetics and slow interfacial charge transfer.[10–13] Second, to design appropriate electrolytes for Mg plating/stripping with high Coulombic efficiency, wide electrochemical window, and good compatibility with the cathodic materials is another great challenge.[14,15] Therefore, to develop advanced cathode materials capable of rapid Mg^{2+} insertion/extraction in suitable electrolytes for reversible Mg plating/stripping is highly desirable.

Since the pioneering work of Chevrel phase compounds (Mo_6S_8) reported by Aurbach et al. in 2000,[16] tremendous efforts have been devoted to develop cathode materials for RMBs, including transition metal oxides (MnO_2, V_2O_5, Mn_3O_4, WO_3, Co_3O_4),[17–21] polyanionic compounds ($Mg_{1.03}Mn_{0.97}SiO_4$, $MgCoSiO_4$),[22,23] and transition metal dichalcogenides (TMDs, such as TiS_2, MoS_2, WSe_2).[24–28] However, most oxides and polyanionic compounds suffer from low capacity and poor cycling performance owing to the strong interactions between divalent Mg^{2+} and O^{2-} in the hosts.[25,29] On the contrary, TMDs are deemed to be a class of promising cathode materials with more favorable kinetics, attributing to the relatively weaker Mg—S or Mg—Se bonds than Mg—O bond.[25,28,30] Nevertheless, layered TMDs also suffer from slow Mg^{2+} ion diffusion due to the narrow interlayer spacing and the high polarity of Mg^{2+}.[31] Recently, it was reported that the interlayer distances of TMDs could be expanded by intercalating guest molecules (water or organic molecules), enlarging the dimension of ion diffusion channels and shielding the Coulombic interactions between Mg^{2+} and the lattice anions of hosts.[13,27] In addition, the intercalated molecules served as interlayer pillars are conducive to maintain the framework of host materials for prolonged cycles.[32,33]

X. L. Xue, R. P. Chen, Dr. C. Z. Yan, P. Y. Zhao, Y. Hu, W. H. Kong, H. N. Lin, L. Wang, Prof. Z. Jin
Key Laboratory of Mesoscopic Chemistry of MOE
Jiangsu Key Laboratory of Advanced Organic Materials
School of Chemistry and Chemical Engineering
Nanjing University
Nanjing 210023, China
E-mail: zhongjin@nju.edu.cn
Dr. C. Z. Yan, Prof. Z. Jin
Shenzhen Research Institute of Nanjing University
Shenzhen 518057, China
The ORCID identification number(s) for the author(s) of this article can be found under https://doi.org/10.1002/aenm.201900145.

DOI: 10.1002/aenm.201900145

Vanadium disulfide (VS_2) is a typical member of layered TMDs with hexagonal structure, which is composed of a metal vanadium layer interleaved with double sulfur slabs and stacked by weak van der Waals force with an interlayer spacing of 5.76 Å.[34,35] This loosely stacked framework with large open channels between the layers makes VS_2 a promising pseudocapacitive candidate because this structure is propitious to the fast ion diffusion and the maintenance of structural integrity during repetitive cycling.[36] In addition, theoretical studies have predicted that monolayer VS_2 is metallic, which is beneficial to the charge transfer.[37] These features endow VS_2 a great potentiality in RMBs. Herein, we report the preparation of expanded VS_2 nanoflowers intercalated with 2-ethylhexylamine molecules as a high-performance cathode material for RMBs. The intercalation of 2-ethylhexylamine molecules on one hand greatly enlarged the interlayer spacing for accelerating ion diffusion, on the other hand shielded the electrostatic interactions between active magnesium species and VS_2 host. To elucidate the detailed reversible magnesium storage mechanism of expanded VS_2, ex situ X-ray diffraction (XRD), transmission electron microscopy (TEM) and X-ray photoelectron spectroscopy (XPS) characterizations are carried out. Furthermore, galvanostatic intermittent titration technique (GITT) and cyclic voltammetry (CV) methods are used to investigate the thermodynamics and reaction kinetics of expanded VS_2 during magnesiation/demagnesiation, confirming the fast Mg^{2+} diffusion rate and high pseudocapacitive contribution accounting for the good performances of magnesium ion storage. According to the previous report,[38] $Mg(HMDS)_2$-$4MgCl_2$/THF is an excellent electrolyte for RMBs. However, its practical application is still limited by the high volatility and flammability of THF. Notably, ionic liquids have been widely used as an efficient additive in the electrolytes of electrochemical energy storage systems, owing to their low melting points, high boiling points, low vapor pressures, high chemical and thermal stability, and good nonflammability, etc.[39,40] Hence, in this work, the $PP_{14}TFSI$ ionic liquid with relatively wide electrochemical window and high ionic conductivity is selected as a co-solvent to improve the physicochemical properties of electrolyte.

2. Results and Discussion

The process for preparing expanded VS_2 nanoflowers is schematically illustrated in **Figure 1**a. The expanded VS_2 nanoflowers with enlarged interlayer spacing were directly synthesized by a one-pot solvothermal method with the assistance of 2-ethylhexylamine served as both solvent and intercalation agent, as detailed in the Experimental section of Supporting Information. As a comparison, the expanded VS_2 nanoflowers were further annealed at 400 °C to removing the 2-ethylhexylamine molecules, to obtain a control sample of annealed VS_2 nanoflowers with normal (recovered) interlayer spacing. Figure 1b,e present the scanning electron microscopy (SEM) images of the as-prepared expanded VS_2 nanoflowers and annealed VS_2 nanoflowers. These two samples with almost the same morphologic features are composed of uniform flower-like nanostructures assembled by numerous nanosheets. As shown in Figure 1c,f, TEM images further demonstrate their hierarchical structures assembled by wrinkled VS_2 nanosheets. From the high-resolution TEM (HRTEM) images in Figure 1d,g, it is found that the expanded VS_2 nanoflowers display a well-defined ultrathin layered structure with an interlayer spacing of 9.93 Å, corresponding to the expanded (001) planes of VS_2; while the annealed VS_2 nanoflowers exhibit a narrowed interlayer spacing of 5.73 Å comparable to normal VS_2. The polycrystalline nature of the as-synthesized samples is confirmed by selected-area electron diffraction (SAED) patterns (the insets of Figure 1d,g). The energy-dispersive X-ray spectra (EDX) and corresponding elemental mappings (Figure 1h,i and Figure S1, Supporting Information) confirm the presence and homogeneous distribution of V, S, C, and N elements in the expanded VS_2 nanoflowers and annealed VS_2 nanoflowers. The EDX analysis of expanded VS_2 nanoflowers displays a higher atomic ratio of N element compared to annealed VS_2 nanoflowers, indicating the realization of 2-ethylhexylamine intercalation.

XRD analysis was used to investigate the crystalline structures of the as-prepared samples (**Figure 2**a). All XRD peaks of annealed VS_2 nanoflowers are consistent with the position of hexagonal VS_2 (JCPDF#36-1139). In contrast, the diffraction peaks of expanded VS_2 nanoflowers are markedly different, showing a sharp peak at 9.28°, and the corresponding interlayer distances of 9.93 Å is assignable to the (001) lattice plane of expanded VS_2.[41,42] The XRD pattern of the expanded VS_2 does not match well with the PDF card, which is because of the insertion of large organic molecules between the layers and thus the positions of some diffraction peaks are changed.[41] For comparison, annealed VS_2 nanoflowers shows the (001) diffraction peak at 15.6° after removing the 2-ethylhexylamine molecules by thermal treatment, possessing the standard interlayer distance of 5.73 Å. It can be deduced that the interlayer distance enlargement of expanded VS_2 nanoflowers is attributed to the intercalation of 2-ethylhexylamine molecules, as evidenced by attenuated total reflectance Fourier transform infrared (ATR-FTIR) spectroscopy in Figure 2b. The peaks at around 3423 and 1615 cm^{-1} are attributed to the stretching and bending vibrations of N—H bonds, respectively. The peaks at 2957, 2926, and 2858 cm^{-1} are assigned to the stretching vibrations of CH, CH_2, and CH_3 groups. The peaks located at 1465 and 1378 cm^{-1} are indexed to the bending vibrations of CH_2 and CH_3 groups. The C—N stretching vibration absorption signals between 1000 and 1400 cm^{-1} are also observed. These results reveal the presence of 2-ethylhexylamine molecules in the as-synthesized expanded VS_2 nanoflowers. To further confirm the successful intercalation of 2-ethylhexylamine molecules in expanded VS_2 nanoflowers, thermogravimetric analysis (TGA) was carried out from 25 to 500 °C in N_2 atmosphere, as presented in Figure S2 of Supporting Information. Compared to that of annealed VS_2 nanoflowers, the TG trace of expanded VS_2 nanoflowers shows a weight loss of 16%, corresponding to the evaporation and thermal decomposition of intercalated 2-ethylhexylamine molecules.[42] In Figure S3a of Supporting Information, the Raman spectra of both expanded and annealed VS_2 nanoflowers present six characteristic bands at 140.4, 192.1, 281.5, 406.6, 687.8, and 991.6 cm^{-1}, well consistent with the previous reports.[43,44]

XPS analysis was further conducted to investigate the chemical compositions and states of the samples (Figure S3b,

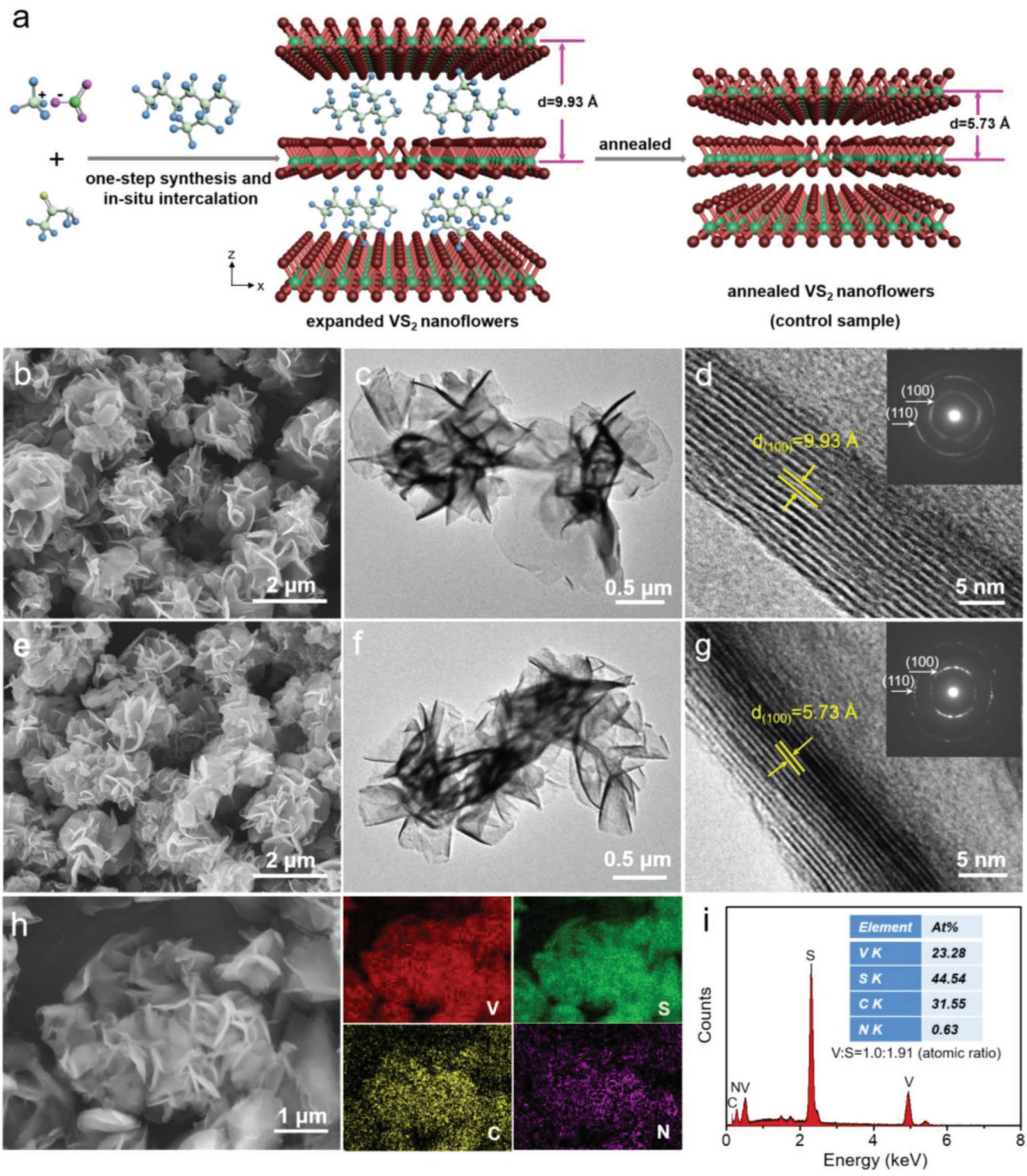

Figure 1. a) Schematic illustration of the one-step synthesis and in situ intercalation process of expanded VS_2 nanoflowers and annealed VS_2 nanoflowers. b,e) SEM, c,f) TEM, and d,g) high-resolution TEM images of expanded VS_2 nanoflowers and annealed VS_2 nanoflowers, respectively. The insets in (d) and (g) are the corresponding SAED patterns. h) Spatial distribution and i) atomic contents of V, S, C, and N elements in interlayer-expanded VS_2 nanoflowers.

Supporting Information). It is observed that all the XPS peaks can be indexed to V, S, C, and N elements. In the high-resolution V 2p spectra, two main peaks at around 524.3 and 516.7 eV are assignable to V $2p_{1/2}$ and V $2p_{3/2}$, corresponding to the V^{4+} state (Figure 2c).[42] In addition, two smaller peaks at around 522.7 and 513.3 eV are observed, indicating the formation of a small amount of V^{2+} species due to the reducibility of organic amines and the strong reducibility of H_2S

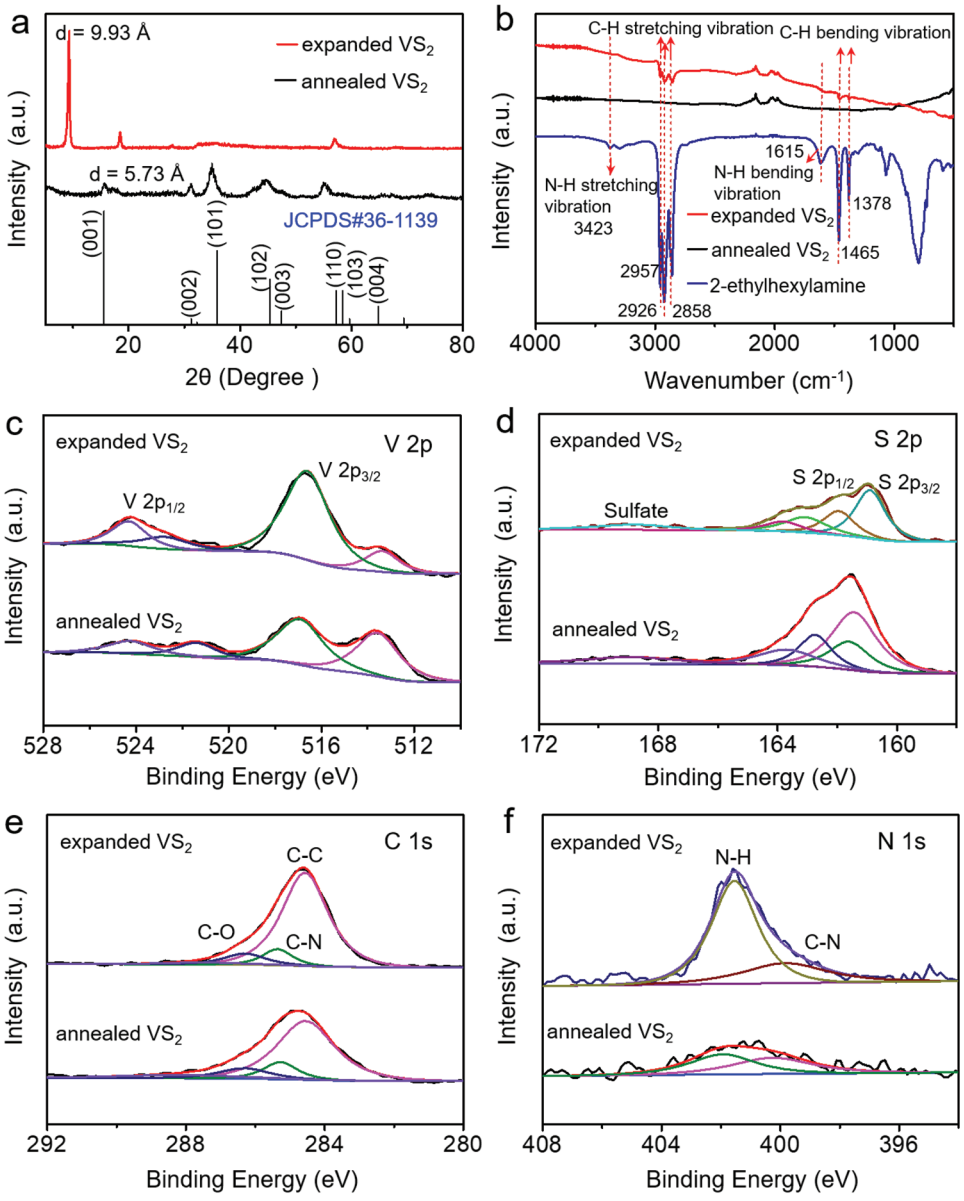

Figure 2. a) XRD patterns of expanded VS_2 nanoflowers and annealed VS_2 nanoflowers, respectively. b) ATR-FTIR spectra of expanded VS_2 nanoflowers, annealed VS_2 nanoflowers, and pure 2-ethylhexylamine, respectively. High-resolution XPS spectra at c) V 2p, d) S 2p, e) C 1s, and f) N 1s regions of expanded VS_2 nanoflowers and annealed VS_2 nanoflowers, respectively.

produced by the decomposition of thioacetamide during the synthesis process.[42,45] The V^{2+} ratio in annealed VS_2 nanoflowers is higher than that in expanded VS_2 nanoflowers, owing to the reduction atmosphere in thermal treatment process. As presented in S 2p spectra (Figure 2d), the two major peaks at around 162.0 and 161.5 eV correspond to S $2p_{1/2}$ and S $2p_{3/2}$ of S^{2-} species.[41,42] The peaks located at about 162.7 and 163.8 eV can be assigned to S_2^{2-} and S^0 species, respectively.[46] The peaks at around 168.9 eV assignable to sulfate reveal the slight oxidization of VS_2 due to exposure to air.[42] Figure 2e shows the C 1s spectra of the samples, in which the peaks at 284.6, 285.4, and 286.3 eV can be attributed to C—C, C—N, and C—O bonds, respectively.[41] The peaks at 401.5 and 399.7 eV in N 1s spectra can be assigned to the N—H and N—C bonds in 2-ethylhexylamine molecules and/or N-doped amorphous carbon after annealing.[41,47] For annealed VS_2, the position of this peak is shifted to a slightly higher energy level (≈402 eV), which is because the thermal decomposition of organic amine molecules when annealed at high temperature has caused chemical environmental change of N species. Notably, the intensity of N signal at 401.5 eV of expanded VS_2 nanoflowers is much stronger than that of annealed VS_2 nanoflowers, indicating the successful intercalation of 2-ethylhexylamine molecules in expanded VS_2 nanoflowers. N_2 adsorption/desorption isotherms were used to determine the specific surface areas of the products, which reveal their type-IV isotherms with a porous structure (Figure S4a, Supporting Information). The BET surface areas of expanded VS_2 and annealed VS_2 are 136

and 177 m^2 g^{-1}, respectively, and the pore size calculations of expanded VS_2 and annealed VS_2 indicate a similar distribution (Figure S4b, Supporting Information). The relatively large specific surface area and highly porous structure are beneficial to the interfacial contact between electrolyte and electrode materials and can provide more active sites for magnesium storage.

The electrolytes were first synthesized and characterized as detailed in the Supporting Information. As presented in Figure S5 of Supporting Information, the TGA curves show that pure $PP_{14}TFSI$ exhibits almost no significant weight loss below 385 °C, indicating its excellent thermal stability. Similarly, the mixed solution of THF and $PP_{14}TFSI$ with a volume ratio of 2:1 begins to lose weight at above 375 °C, while the boiling point of pure THF is only 66 °C, demonstrating that the addition of $PP_{14}TFSI$ can effectively inhibit the solvent volatilization in electrolyte. Moreover, the Mg plating/stripping behaviors in $Mg(HMDS)_2$-$4MgCl_2$/THF and $Mg(HMDS)_2$-$4MgCl_2$/2THF-$PP_{14}TFSI$ have also been analyzed by CV. Although the overpotential of Mg plating/stripping in $Mg(HMDS)_2$-$4MgCl_2$/2THF-$PP_{14}TFSI$ is slightly higher than that in $Mg(HMDS)_2$-$4MgCl_2$/THF, the Mg plating/stripping currents in the former electrolyte are greatly higher than that in the latter, indicating the addition of $PP_{14}TFSI$ can significantly improve the Mg plating/stripping performance (Figure S6a, Supporting Information). Besides, The CV curves measured with Pt foil as working electrode and Mg foil as both counter and reference electrodes also display that the electrochemical window of $Mg(HMDS)_2$-$4MgCl_2$/2THF-$PP_{14}TFSI$ is wider than that of $Mg(HMDS)_2$-$4MgCl_2$/THF, indicating the better oxidation stability of the former. To further investigate the Mg plating/stripping behavior of $Mg(HMDS)_2$-$4MgCl_2$/2THF-$PP_{14}TFSI$, the chronopotentiometry was conducted by the coin cells with Mo as positive electrode and Mg as negative electrode. As shown in Figure S6b of Supporting Information, the Coulombic efficiency of the first cycle is 94.6% and finally stabilizes at about 98.6%, indicating its good capability for stable Mg plating/stripping.

To examine the electrochemical properties of expanded VS_2 and annealed VS_2 nanoflowers, CV analysis and galvanostatic discharge/charge cycling were conducted. The CV profiles of expanded VS_2 nanoflowers (**Figure 3**a), except the first two cycles, show two pairs of redox peaks at 1.37/1.18 and 0.80/0.56 V, in which the former is corresponding to the active magnesium species intercalation/deintercalation and the latter is assignable to the magnesium conversion reaction. The first two cycles of CV curves display apparent differences compared with the latter cycles, indicating that the first few cycles of expanded VS_2 electrode undergo irreversible reactions. Meanwhile, another reduction peak at about 1.60 V is observed, which should be ascribed to the reactions in the first few cycles of activation process and the reactions between organic amine and electrolyte. The CV curves of expanded VS_2 electrode after cycled at the current density of 100 mA g^{-1} for 10 cycles in Figure S7 of Supporting Information show that the reduction peak at about 1.60 V disappears, indicating the disappearance of these side reactions, which is also a good explanation for the capacity increase in the following cycles. Notably, compared to the expanded VS_2 electrode, the CV profile of annealed VS_2 electrode exhibits no obvious redox peaks and significantly decreased peak currents, implying the inferior electrochemical performance of annealed VS_2 with almost negligible active magnesium species intercalation/deintercalation capability (Figure S8a, Supporting Information). Figure 3b presents the discharge/charge performances of expanded VS_2 and annealed VS_2 electrodes at the current density of 100 mA g^{-1}. With about 10 cycles of activation, a highly reversible discharge capacity of 245 mAh g^{-1} was obtained by expanded VS_2 electrode and retained 78% of this value after 100 cycles. The Coulombic efficiency of the first cycle is 59.3% with the initial discharge and charge capacities of 116 and 69 mAh g^{-1}, respectively, and it is greatly improved to about 104% starting from the ninth cycle, which could be attributed to the polarization and activation of the electrode in the first few cycles. For comparison, the annealed VS_2 electrode only exhibits a poor discharge capacity of about 30 mAh g^{-1}, because the intrinsic narrow interlayer spacing and strong electrostatic interaction seriously hindered the magnesium storage.

Figure 3c shows the galvanostatic discharge/charge profiles of the expanded VS_2 electrode at various current densities. The discharge profiles exhibit a plateau behavior, corresponding to the intercalation of active magnesium species. The discharge plateau is still visible at high current rate of 2000 mA g^{-1}, despite of showing a slight decline of the platform voltage. In contrast, the galvanostatic discharge/charge profiles of annealed VS_2 electrode cannot display a plateau behavior (Figure S8b, Supporting Information), which is in accordance with the CV profiles. The expanded VS_2 electrode achieves a high discharge capacity of 249 mAh g^{-1} at 100 mA g^{-1} after 10 cycles of activation. When the current rate increases stepwise, the expanded VS_2 electrode exhibits average reversible discharge capacities of 212, 179, 140, and 102 mAh g^{-1} at 300, 500, 1000, and 2000 mA g^{-1}, respectively (Figure 3d). Moreover, when the current rate is reduced stepwise back to 100 mA g^{-1}, the specific capacity of expanded VS_2 electrode recovers to 232 mAh g^{-1}, indicating the good tolerance of host material during magnesiation/demagnesiation processes. In contrast, the annealed VS_2 electrode delivers very poor discharge capacities at the same current densities (Figure 3d). As shown in Figure S9 and Table S1 of Supporting Information, the rate performance of expanded VS_2 nanoflowers is very competitive among the previously reported cathode materials for RMBs, especially at high current densities.

To evaluate the long-term cycling stability, the RMBs based on the expanded VS_2 and annealed VS_2 cathodes are cycled at a high current density of 1000 mA g^{-1}. As presented in Figure 3e, after nearly 10 cycles of activation, the discharge and charge capabilities of expanded VS_2 cathode are gradually increased from 81 and 63 mAh g^{-1} to 129 and 132 mAh g^{-1}, respectively, corresponding to the increase of Coulombic efficiency from 77% to nearly 102%. After 600 cycles, the discharge capacity of expanded VS_2 electrode still maintains at 90 mAh g^{-1}, with a capacity retention of about 70% and Coulombic efficiency of 102%. The Coulombic efficiency at lower current density is greater than 100%, while it is improved to nearly 100% at high current density, which could be owing to the self-discharge phenomenon at lower current density, similar to the results reported in previous works.[48,49] The cycling stability of expanded VS_2 nanoflowers is remarkable among the reported Mg-storage cathode materials (Table S1, Supporting

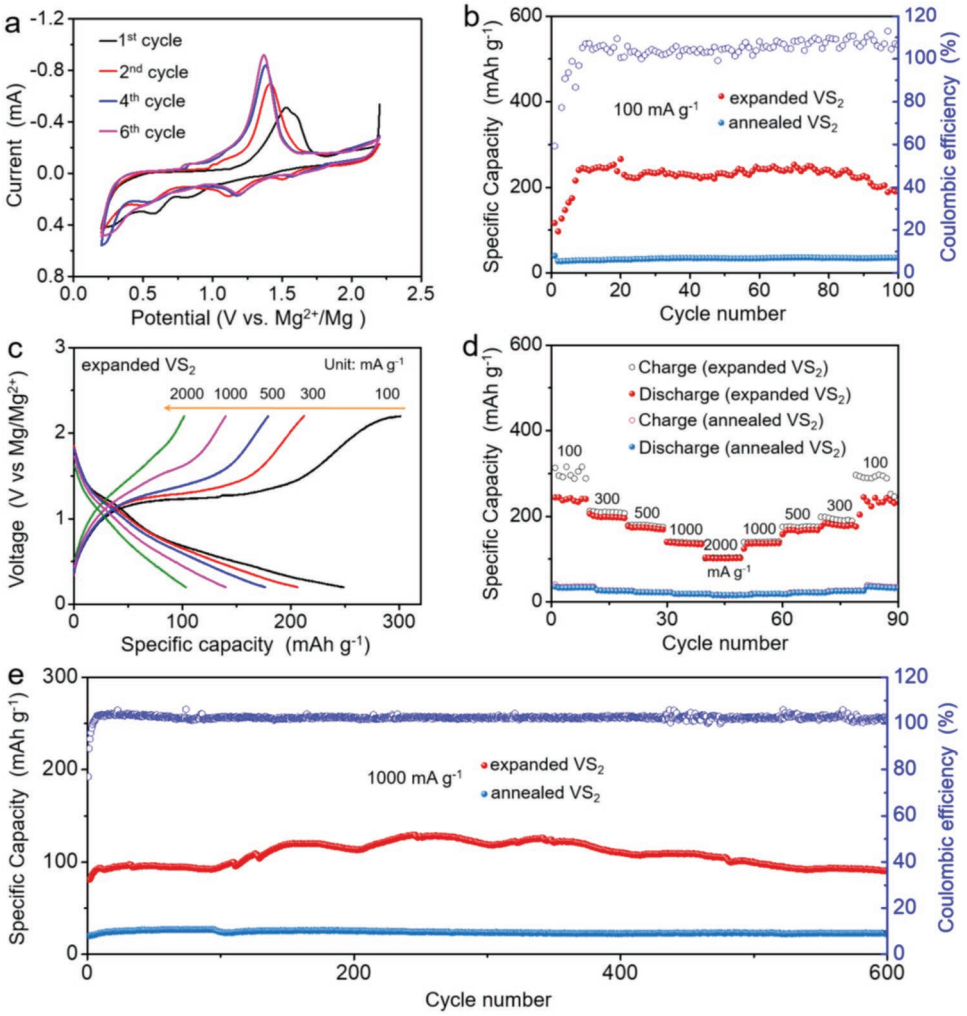

Figure 3. a) CV curves of expanded VS_2 electrode at a scan rate of 0.2 mV s^{-1} in the voltage range of 0.2–2.2 V versus Mg^{2+}/Mg. b) Cycling performances and Coulombic efficiencies of expanded VS_2 and annealed VS_2 electrodes tested at a current density of 100 mA g^{-1}, respectively. c) Galvanostatic discharge/charge profiles at various current densities. d) Rate capabilities of expanded VS_2 and annealed VS_2 electrodes at the current densities from 100 to 2000 mA g^{-1}. e) Long-term cycling performances of expanded VS_2 and annealed VS_2 electrodes at a current density of 1000 mA g^{-1} for 600 cycles, respectively.

Information). In comparison, the annealed VS_2 cathode only delivers an average discharge capacity of only 22 mAh g^{-1} for 600 cycles with a Coulombic efficiency of nearly 101%. In addition, to investigate the morphology characteristics variation of expanded VS_2 electrode, the SEM image and XRD pattern after 10 discharge/charge cycles at 100 mA g^{-1} were measured. As shown in Figure S10 of Supporting Information, the expanded VS_2 still maintains a sheet structure after 10 cycles and the XRD peaks show very slight shifts, suggesting the good structural stability. This structural integrity of expanded VS_2 during discharge/charge process is beneficial to the long cycling life.

It has been suggested that the expanded intercalation-type materials may store $MgCl^+$ ions rather than Mg^{2+} ion.[13,50] Therefore, here we also investigated the active magnesium species inserted in the expanded VS_2 electrode based on $Mg(HMDS)_2$-4$MgCl_2$/2THF-$PP_{14}TFSI$ electrolyte by XPS and EDS analysis. As presented in Figure S11a,b of Supporting Information, compared with pristine expanded VS_2 electrode, the Mg 2s and Cl 2p signals concurrently appeared when discharged to 0.6 V and the peak intensities obviously increased when fully discharged to 0.2 V, and the peak intensity synchronously decreased again upon charging back to 2.2 V, indicating the simultaneous insertion/extraction of Mg and Cl species into/from the expanded VS_2 electrode. To further investigate the types of active Mg species, EDS measurements were also conducted to analyze the Mg/Cl atomic ratios at different states. Notably, the Mg/Cl atomic ratios at all of the different discharge/charge states are always larger than 1, which is in accordance with the atomic concentration table of XPS analysis (Table S2, Supporting Information). Therefore, it is possible that both $MgCl^+$ and desolvated Mg^{2+} ions may simultaneously participate the cation insertion/extraction processes of expanded VS_2 electrode.[51]

The electrochemical impedance spectra (EIS) of expanded VS_2 and annealed VS_2 cathodes are provided in Figure S12a of Supporting Information. The semicircle radius in the

high-frequency region of expanded VS_2 electrode is smaller than that of annealed VS_2 electrode, suggesting the smaller charge transfer resistance of expanded VS_2 at electrode–electrolyte interface, which is beneficial to the rate performance. Moreover, the EIS plot of the expanded VS_2 electrode after 10th discharge/charge cycles at 100 mA g^{-1} was also measured. As shown in Figure S12b of Supporting Information, the semicircle radius in the high-frequency region is greatly decreased after 10th cycles, which is probably because the electrode undergoes an activation process in the initial cycles and/or the generation of metallic vanadium during the conversion reaction stage. To probe the diffusivity of active magnesium species ions in expanded VS_2 nanoflowers, the discharge and charge GITT curves of expanded VS_2 electrode at 50 mA g^{-1} after activation of 5 cycles were measured, as shown in **Figure 4**a. Herein, for convenience of calculation, the Mg^{2+} was considered as the active species to calculate the ion diffusion coefficient due to the uncertainty of the $Mg^{2+}/MgCl^+$ ratio. The Mg^{2+} ion diffusivity can be calculated according to the following equation[52]

$$D_{Mg^{2+}} = \frac{4}{\pi\tau}\left(\frac{m_B V_M}{M_B S}\right)^2\left(\frac{\Delta E_s}{\Delta E_t}\right)^2 \quad (1)$$

where τ is the constant current pulse time, m_B, V_B, and M_B denote the mass, molar volume, and molar mass of the active material, respectively, S is the surface area of electrode–electrolyte interface, ΔE_s is the voltage difference between the steady state and the original state, and ΔE_t is the total voltage change during a current pulse τ excluding the iR drop. From Figure 4b, it can be observed that the Mg^{2+} ion diffusion coefficient (D_{Mg}) is decreased from 7.58×10^{-11} to 6.03×10^{-13} cm^2 s^{-1} when the Mg content (x) inserted in expended VS_2 is increased from 0.034 to 0.240. As x increases to above 0.240, the Mg^{2+} ion diffusivity of discharge process increases again and reaches to a relatively stable level of $\approx 7.00 \times 10^{-12}$ cm^2 s^{-1}. These results indicate that the Mg^{2+} ion diffusivity is relatively high in expended VS_2.

To further understand the superior magnesium storage abilities of expanded VS_2 nanoflowers, the electrochemical kinetic analysis based on CV method was employed to investigate the pseudocapacitance contribution to the total capacity according to a previous approach reported by Dunn and co-workers.[53] Figure 4c shows the typical CV curves of expanded VS_2 electrode at different scan rates from 0.2 to 2.0 mV s^{-1} between 0.2 and 2.2 V. With the increase of scan rates, the redox peaks of CV curves exhibit subtle shifts. The relationship between the measured currents (i) and the scan rates (v) was also investigated by the following equations[53]

$$i(V) = a v^b \quad (2)$$

$$\log i(V) = b \log v + \log a \quad (3)$$

where the measured current i and the sweep rate v obey a power law. Both a and b are adjustable parameters and b-values are derived from the slope of the curve of log i versus log v on the basis of Equation (3). The b-value of 1.0 signifies that the electrode is controlled by capacitive response, while $b = 0.5$ indicates the diffusion process is dominating.[53,54] The calculated b-values of discharge and charge processes at different potentials for expanded VS_2 electrode are presented in Figure 4d,e. At the potentials of 0.90 and 1.15 V in the anodic process, the b-values are 0.97 and 0.76, indicating that the discharge storage mainly comes from intercalation pseudocapacitance, thus leading to the fast active Mg species diffusion. During the charge process, the b-values are 0.97 and 0.53 at the potentials of 1.43 and 1.57 V, indicating that both the capacitive response and the diffusion process contribute to the capacity. Therefore, it is reasonable to deduce that the magnesium storage behavior of expanded VS_2 electrode is mainly controlled by capacitive and diffusion processes. Moreover, the contributions of capacitive and diffusion processes can be quantified according to the following equations[53]

$$i(V) = k_1 v + k_2 v^{1/2} \quad (4)$$

$$i(V) v^{-1/2} = k_1 v^{1/2} + k_2 \quad (5)$$

where $k_1 v$ and $k_2 v^{1/2}$ stand for the capacitive and diffusion effects, respectively. As shown in Figure 4f, the k_1-values at different potentials are obtained from the slopes of the plots of $v^{1/2}$ versus $i(V)v^{-1/2}$. As depicted by the red shaded area (Figure 4g), the capacitance contribution was calculated to be 64% at 1.0 mV s^{-1}. From Figure 4h, the ratios of capacitive contribution at the san rates of 0.2, 0.6, 1.0, and 2.0 mV s^{-1} are 53%, 58%, 64%, and 78%, respectively, revealing that the electrochemical behavior of expanded VS_2 electrode is mainly controlled by the capacitive effect, while the diffusion process also contributes to some capacity, which accounts for the excellent rate capability.

To further understand the magnesiation/demagnesiation mechanism of expanded VS_2 nanoflowers, ex situ XRD, HRTEM, XPS, ICP-OES, and EDX characterizations were systematically performed at the second cycles to identify the possible phases. The XRD patterns of expanded VS_2 electrode at different discharge/charge states are shown in **Figure 5**a,b. When discharged from 2.2 to 0.6 V, the (001) and (002) diffraction peaks are getting weaker and shift to lower angles, suggesting the interlayer spacing expansion of host material during the Mg-ion insertion. The XRD peaks of expanded VS_2 are disappeared when the electrode is discharged from 0.4 to 0.2 V, meanwhile a weak diffraction peak of MgS at 29.7° and a new peak of metallic V at 42.1° are emerged. When the electrode is further fully charged to 2.2 V, all the peaks of VS_2 reappear again; However, the (001) and (002) peaks shift to lower angles compared with the pristine state, indicating the further expansion of interlayer distances. The XRD peak intensities and full width at half-maximums (FWHMs) of expanded VS_2 nanoflowers are well recovered after fully charged to 2.2 V, indicating a highly reversible structure evolution. These results were further confirmed by ex situ HRTEM analysis. When discharged to 0.6 V, the lattice spacing of (001) planes increases from 9.93 to 10.70 Å, verifying the intercalation reaction mechanism and in agreement with the ex situ XRD results (Figure 5e). Notably, the interlayer spacing is further increased to 10.90 Å at 0.4 V, meanwhile a new lattice spacing of 3.00 Å belonging to MgS is observed, demonstrating the co-existence of magnesium

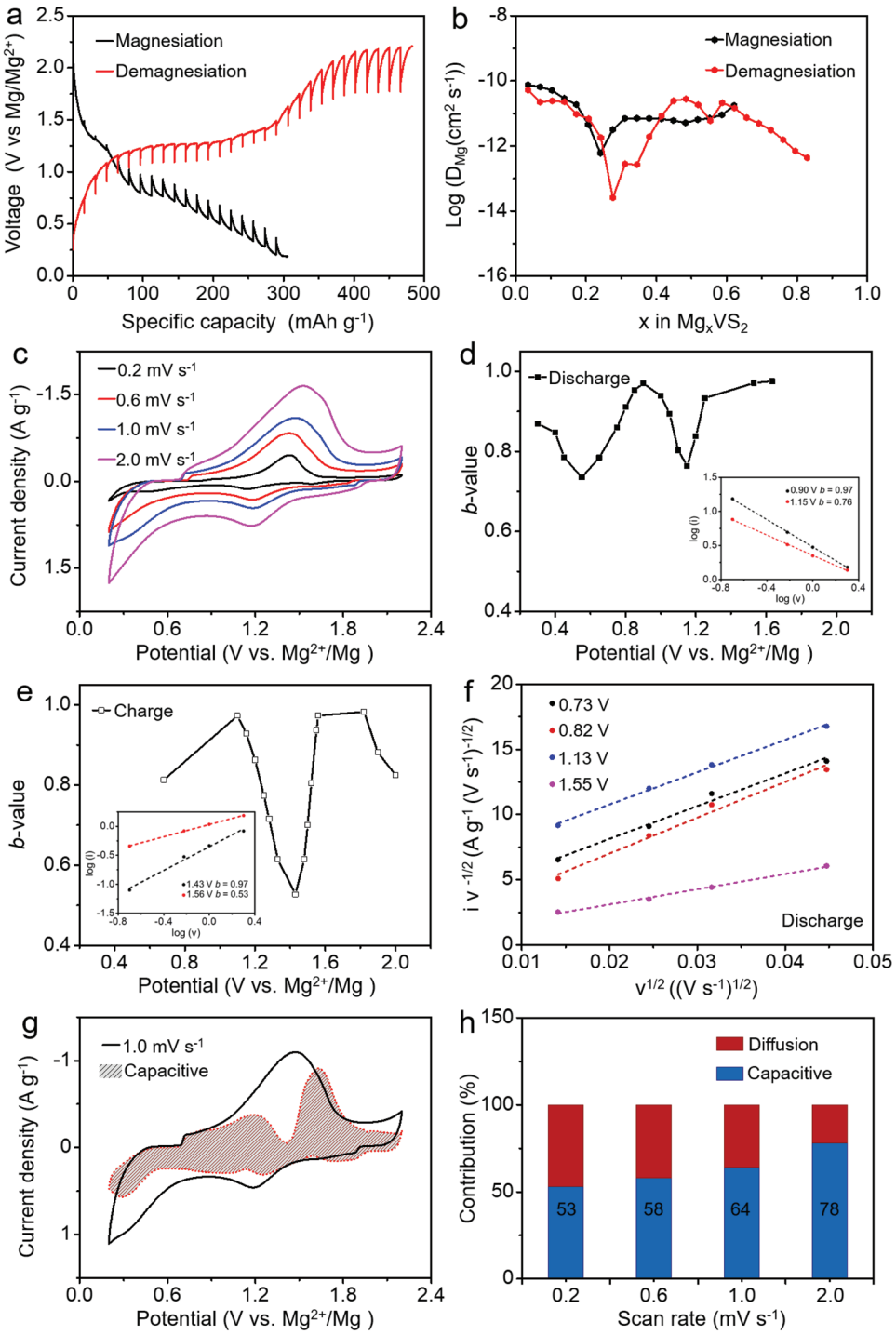

Figure 4. a) Potential response of expanded VS_2 electrode during GITT measurement at a constant current density of 50 mA g^{-1}. b) The logarithm of calculated diffusion coefficient for Mg^{2+} ion (D_{Mg}) versus the Mg content (x) inserted in expended VS_2. c) CV curves of expanded VS_2 electrode at different scan rates. Calculated b-values as a function of potential for d) discharged and e) charged sweeps. The inset shows the power law relationships between the logarithm currents and the logarithm sweep rates. f) Curves of $v^{1/2}$ versus $iv^{-1/2}$, in which v varies from 0.2 to 2.0 mV s^{-1}. g) Pseudocapacitive contribution (the red shaded region) to the total capacity at 1.0 mV s^{-1}. h) Normalized contribution ratio of pseudocapacitive contribution to the total capacity at different sweep rates.

intercalation and conversion reaction (Figure 5f). When fully discharged to 0.2 V, apart from the lattice spacing at 10.90 Å corresponding to the (100) planes of expanded VS_2, the lattice fringes of the MgS (111) planes at 3.00 Å and the metallic V (110) planes at 2.14 Å can also be seen (Figure 5g), indicating that a portion of VS_2 has been reduced to metallic V. When fully

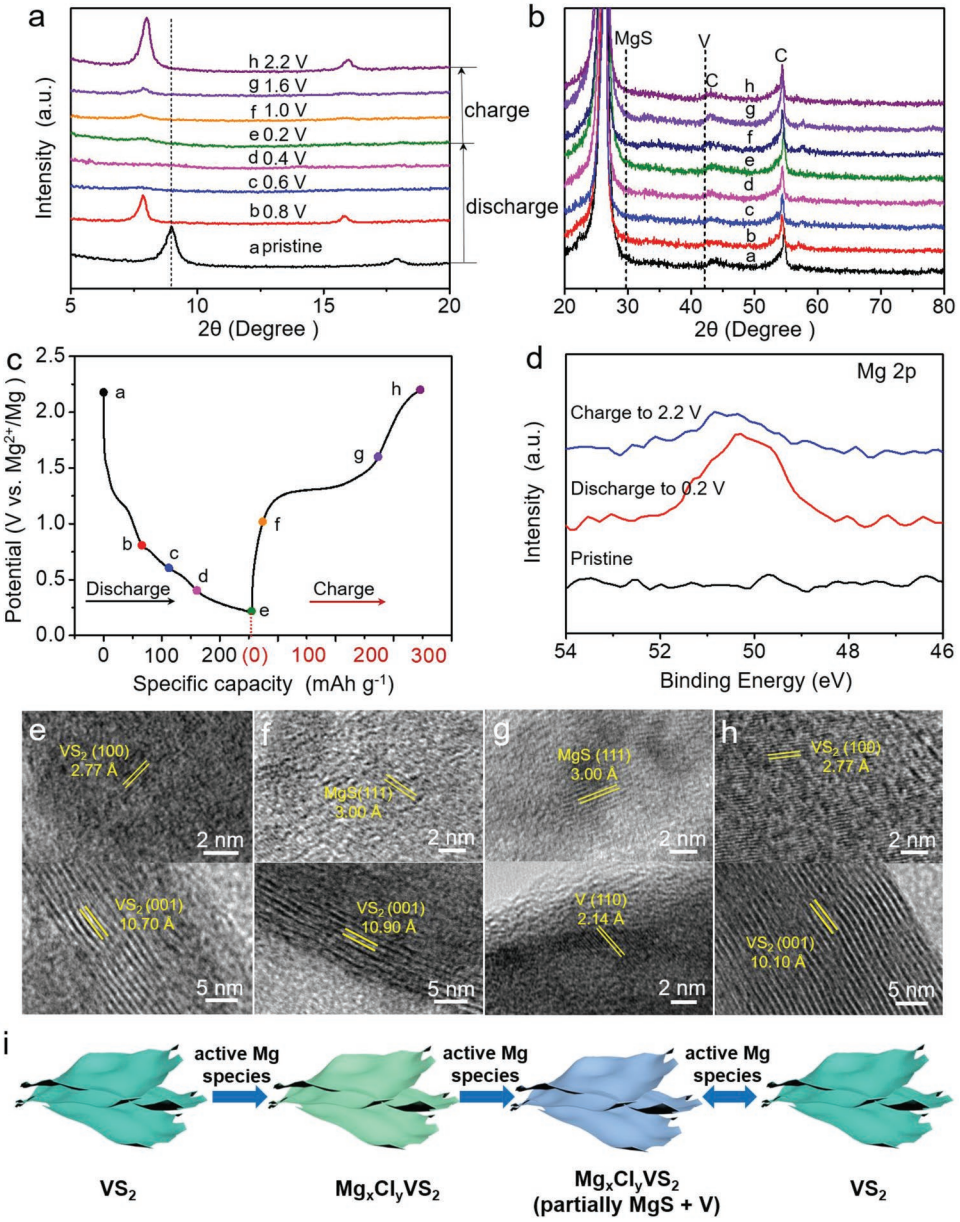

Figure 5. Structural characterizations of expanded VS_2 nanoflowers during the magnetization/demagnetization processes. a,b) Ex situ XRD patterns and c) the corresponding specific capacities of expanded VS_2 electrodes at different discharge/charge states. d) Ex situ high-resolution XPS spectra at Mg 2p region measured at the pristine state, after discharged to 0.2 V and after charged to 2.2 V, respectively. HRTEM images of expanded VS_2 nanoflowers at different discharge/charge states: e) discharged to 0.6 V, f) discharged to 0.4 V, g) fully discharged to 0.2 V, and h) fully charged to 2.2 V. i) Schematic reversible storage mechanism of active magnesium species in expanded VS_2 nanoflowers.

charged back to 2.2 V, the HRTEM images in Figure 5h display clear lattice spacings of 2.77 and 10.10 Å, corresponding to the (100) and (001) plane of expanded VS_2. Moreover, the variation of magnesiation/demagnesiation degree is further confirmed by ex situ XPS spectra. As presented in Figure 5d, the intensity of Mg 2p peak at the fully discharged state is much higher than those at the pristine state and the fully charged state, indicating the reversible insertion/extraction of active magnesium species into/from expanded VS_2. To further confirm the magnesium storage mechanism, the variation of the V 2p XPS peaks at different states were tracked (Figure S13, Supporting Information). It can be seen that low-valence V^{2+} and V^{3+} species are observed at the fully discharged state, which illustrates the valence of V decreases with the insertion of cations. In addition, a small peak of V^0 is also found at the fully discharged state, corresponding to the product of partial conversion reaction. When fully charged, V^{4+} becomes the major V species, indicating the good reversibility of the intercalation and conversation reactions in expanded VS_2 electrode. In addition, the presence of V^{5+} is attributed to the unavoidable oxidation of VS_2 exposed to the air when tested. Similarly, ICP-OES and EDS measurements (Tables S3 and S4, Supporting Information) also

show the obvious variation of Mg/V atomic ratio during the discharge/charge cycles. All these characterization results demonstrate that the reaction mechanism of magnesium storage in expanded VS_2 nanoflowers is mainly active magnesium species intercalation, followed by the partial conversion reaction at the end of the discharge processes (below 0.4 V), as illustrated in Figure 5i.

3. Conclusion

In summary, here we report the single-step synthesis of interlayer-expanded VS_2 nanoflowers as a high-performance cathode material for RMBs. The 2-ethylhexylamine molecules intercalated in expanded VS_2 nanoflowers can effectively widen the ionic channels, providing more active sites for active magnesium species intercalation and boosting the ion transport by alleviating undesirable electrostatic interactions between the active magnesium species and the anions of host material. Simultaneously, as interstitial pillars, the 2-ethylhexylamine molecule intercalants are conducive to maintain the integrity of host framework, thus in favor of the long-term discharge/charge cycles. Through systematic ex situ characterizations of the structural variation during cycling processes, we confirm that the magnesium storage capacity of expanded VS_2 is mainly attributed to the intercalation pseudocapacitance, while the conversion reaction provides a small portion of contribution. Our work presents an intrinsic understanding of the Mg-storage mechanism in interlayer-expanded layered compounds of TMDs. It is also concluded that the reasonable regulation of interlayer spacing represents an efficient method to developing multivalent-ion batteries with high rate capability and long cycling life.

Supporting Information

Supporting Information is available from the Wiley Online Library or from the author.

Acknowledgements

X. L. X. and R. P. C. contributed equally to this work. This work was supported by National Key R&D Program of China (2017YFA0208200, 2016YFB0700600, 2015CB659300), Projects of NSFC (21872069, 51761135104, 21573108), Natural Science Foundation of Jiangsu Province (BK20180008, BK20150571), High-Level Entrepreneurial and Innovative Talents Program of Jiangsu Province, and Fundamental Research Funds for the Central Universities.

Conflict of Interest

The authors declare no conflict of interest.

Keywords

cathode materials, expanded vanadium disulfide nanoflowers, high rate capability, intercalation pseudocapacitance, rechargeable magnesium batteries

Received: January 15, 2019
Revised: April 2, 2019
Published online:

[1] B. Dunn, H. Kamath, J. M. Tarascon, *Science* **2011**, *334*, 928.
[2] J. Hassoun, S. Panero, P. Reale, B. Scrosati, *Adv. Mater.* **2009**, *21*, 4807.
[3] Y. Tang, Y. Zhang, W. Li, B. Ma, X. Chen, *Chem. Soc. Rev.* **2015**, *44*, 5926.
[4] N. Yabuuchi, K. Kubota, M. Dahbi, S. Komaba, *Chem. Rev.* **2014**, *114*, 11636.
[5] J. Muldoon, C. B. Bucur, T. Gregory, *Chem. Rev.* **2014**, *114*, 11683.
[6] H. D. Yoo, I. Shterenberg, Y. Gofer, G. Gershinsky, N. Pour, D. Aurbach, *Energy Environ. Sci.* **2013**, *6*, 2265.
[7] R. Mohtadi, F. Mizuno, *Beilstein J. Nanotechnol.* **2014**, *5*, 1291.
[8] C. Ling, D. Banerjee, M. Matsui, *Electrochim. Acta* **2012**, *76*, 270.
[9] S. B. Son, T. Gao, S. P. Harvey, K. X. Steirer, A. Stokes, A. Norman, C. Wang, A. Cresce, K. Xu, C. Ban, *Nat. Chem.* **2018**, *10*, 532.
[10] M. M. Huie, D. C. Boc, E. S. Takeuchi, A. C. Marschilok, K. J. Takeuchi, *Coord. Chem. Rev.* **2015**, *287*, 15.
[11] M. Liu, Z. Rong, R. Malik, P. Canepa, A. Jain, G. Ceder, K. A. Persson, *Energy Environ. Sci.* **2015**, *8*, 964.
[12] E. Levi, M. D. Levi, O. Chasid, D. Aurbach, *J. Electroceram.* **2009**, *22*, 13.
[13] H. D. Yoo, Y. Liang, H. Dong, J. Lin, H. Wang, Y. Liu, L. Ma, T. Wu, Y. Li, Q. Ru, Y. Jing, Q. An, W. Zhou, J. Guo, J. Lu, S. T. Pantelides, X. Qian, Y. Yao, *Nat. Commun.* **2017**, *8*, 339.
[14] J. H. Ha, J. H. Cho, J. H. Kim, B. W. Cho, S. H. Oh, *J. Power Sources* **2017**, *355*, 90.
[15] M. Xu, S. Lei, J. Qi, Q. Dou, L. Liu, Y. Lu, Q. Huang, S. Shi, X. Yan, *ACS Nano* **2018**, *12*, 3733.
[16] D. Aurbach, Z. Lu, A. Schechter, Y. Gofer, H. Gizbar, R. Turgeman, Y. Cohen, M. Moshkovich, E. Levi, *Nature* **2000**, *407*, 724.
[17] R. Zhang, X. Yu, K. W. Nam, C. Ling, T. S. Arthur, W. Song, A. M. Knapp, S. N. Ehrlich, X. Q. Yang, M. Matsui, *Electrochem. Commun.* **2012**, *23*, 110.
[18] Y. Cheng, Y. Shao, V. Raju, X. Ji, B. L. Mehdi, K. S. Han, M. H. Engelhard, G. Li, N. D. Browning, K. T. Mueller, J. Liu, *Adv. Funct. Mater.* **2016**, *26*, 3446.
[19] L. Wang, K. Asheim, P. E. Vullum, A. M. Svensson, F. Vullum-Bruer, *Chem. Mater.* **2016**, *28*, 6459.
[20] R. Wang, C. C. Chung, Y. Liu, J. L. Jones, V. Augustyn, *Langmuir* **2017**, *33*, 9314.
[21] T. E. Sutto, T. T. Duncan, *Electrochim. Acta* **2012**, *80*, 413.
[22] Z. Feng, J. Yang, Y. NuLi, J. Wang, *J. Power Sources* **2008**, *184*, 604.
[23] Q. D. Truong, M. K. Devaraju, I. Honma, *J. Power Sources* **2017**, *361*, 195.
[24] Z. L. Tao, L. N. Xu, X. L. Gou, J. Chen, H. T. Yuan, *Chem. Commun.* **2004**, *0*, 2080.
[25] X. Sun, P. Bonnick, L. F. Nazar, *ACS Energy Lett.* **2016**, *1*, 297.
[26] Y. Liang, R. Feng, S. Yang, H. Ma, J. Liang, J. Chen, *Adv. Mater.* **2011**, *23*, 640.
[27] Y. Liang, H. D. Yoo, Y. Li, J. Shuai, H. A. Calderon, F. C. Robles Hernandez, L. C. Grabow, Y. Yao, *Nano Lett.* **2015**, *15*, 2194.
[28] B. Liu, T. Luo, G. Mu, X. Wang, D. Chen, G. Shen, *ACS Nano* **2013**, *7*, 8051.
[29] E. Levi, Y. Gofer, D. Aurbach, *Chem. Mater.* **2010**, *22*, 860.
[30] X. Sun, P. Bonnick, V. Duffort, M. Liu, Z. Rong, K. A. Persson, G. Ceder, L. F. Nazar, *Energy Environ. Sci.* **2016**, *9*, 2273.
[31] Y. Wang, R. Chen, T. Chen, H. Lv, G. Zhu, L. Ma, C. Wang, Z. Jin, J. Liu, *Energy Storage Mater.* **2016**, *4*, 103.
[32] S. Kim, K. W. Nam, S. Lee, W. Cho, J. S. Kim, B. G. Kim, Y. Oshima, J. S. Kim, S. G. Doo, H. Chang, D. Aurbach, *Angew. Chem.* **2015**, *127*, 15309.
[33] H. J. Lee, J. Shin, J. W. Choi, *Adv. Mater.* **2018**, *30*, 1705851.
[34] J. Feng, X. Sun, C. Wu, L. Peng, C. Lin, S. Hu, J. Yang, Y. Xie, *J. Am. Chem. Soc.* **2011**, *133*, 17832.
[35] J. Feng, L. Peng, C. Wu, X. Sun, S. Hu, C. Lin, J. Dai, J. Yang, Y. Xie, *Adv. Mater.* **2012**, *24*, 1969.

[36] R. Sun, Q. Wei, J. Sheng, C. Shi, Q. An, S. Liu, L. Mai, *Nano Energy* **2017**, *35*, 396.
[37] Y. Jing, Z. Zhou, C. R. Cabrera, Z. Chen, *J. Phys. Chem. C* **2013**, *117*, 25409.
[38] C. Liao, N. Sa, B. Key, A. K. Burrell, L. Cheng, L. A. Curtiss, J. T. Vaughey, J. J. Woo, L. Hu, B. Pan, Z. Zhang, *J. Mater. Chem. A* **2015**, *3*, 6082.
[39] M. Galiński, A. Lewandowski, I. Stępniak, *Electrochim. Acta* **2006**, *51*, 5567.
[40] M. Watanabe, M. L. Thomas, S. Zhang, K. Ueno, T. Yasuda, K. Dokko, *Chem. Rev.* **2017**, *117*, 7190.
[41] Z. T. Shi, W. Kang, J. Xu, Y. W. Sun, M. Jiang, T. W. Ng, H. T. Xue, D. Y. W. Yu, W. Zhang, C. S. Lee, *Nano Energy* **2016**, *22*, 27.
[42] J. Zhang, C. Zhang, Z. Wang, J. Zhu, Z. Wen, X. Zhao, X. Zhang, J. Xu, Z. Lu, *Small* **2018**, *14*, 1703098.
[43] P. He, M. Yan, G. Zhang, R. Sun, L. Chen, Q. An, L. Mai, *Adv. Energy Mater.* **2017**, *7*, 1601920.
[44] J. Zhou, L. Wang, M. Yang, J. Wu, F. Chen, W. Huang, N. Han, H. Ye, F. Zhao, Y. Li, Y. Li, *Adv. Mater.* **2017**, *29*, 1702061.
[45] M. Naguib, J. Halim, J. Lu, K. M. Cook, L. Hultman, Y. Gogotsi, M. W. Barsoum, *J. Am. Chem. Soc.* **2013**, *135*, 15966.
[46] Y. Xue, Z. Zuo, Y. Li, H. Liu, Y. Li, *Small* **2017**, *13*, 1700936.
[47] A. Anto Jeffery, C. Nethravathi, M. Rajamathi, *J. Phys. Chem. C* **2014**, *118*, 1386.
[48] N. Wu, Y. C. Lyu, R. J. Xiao, X. Yu, Y. X. Yin, X. Q. Yang, H. Li, L. Gu, Y. G. Guo, *NPG Asia Mater.* **2014**, *6*, e120.
[49] Z. Zhao-Karger, R. Liu, W. Dai, Z. Li, T. Diemant, B. P. Vinayan, C. B. Minella, X. Yu, A. Manthiram, R. J. Behm, M. Ruben, M. Fichtner, *ACS Energy Lett.* **2018**, *3*, 2005.
[50] L. Zhou, Q. Liu, Z. Zhang, K. Zhang, F. Xiong, S. Tan, Q. An, Y. M. Kang, Z. Zhou, L. Mai, *Adv. Mater.* **2018**, *30*, 1801984.
[51] L. C. Merrill, J. L. Schaefer, *Langmuir* **2017**, *33*, 9426.
[52] Y. Li, Y. Liang, F. C. R. Hernandez, H. D. Yoo, Q. An, Y. Yao, *Nano Energy* **2015**, *15*, 453.
[53] J. Wang, J. Polleux, J. Lim, B. Dunn, *J. Phys. Chem. C* **2007**, *111*, 14925.
[54] V. Augustyn, J. Come, M. A. Lowe, J. W. Kim, P. L. Taberna, S. H. Tolbert, H. D. Abruna, P. Simon, B. Dunn, *Nat. Mater.* **2013**, *12*, 518.